Planar Hall effect in the quasi-one-dimensional topological superconductor $TaSe_3$

X. C. Yang,[1,2] X. Luo,[1,*] J. J. Gao,[1,2] Z. Z. Jiang,[1,2] W. Wang,[1,2] T. Y. Wang,[1,2] J. G. Si,[1,2] C. Y. Xi,[3] W. H. Song,[1] and Y. P. Sun[3,1,4,†]

[1]*Key Laboratory of Materials Physics, Institute of Solid State Physics, HFIPS, Chinese Academy of Sciences, Hefei 230031, China*

[2]*Science Island Branch of Graduate School, University of Science and Technology of China, Hefei 230026, China*

[3]*Anhui Province Key Laboratory of Condensed Matter Physics at Extreme Conditions, High Magnetic Field Laboratory, HFIPS, Chinese Academy of Sciences, Hefei 230031, China*

[4]*Collaborative Innovation Center of Advanced Microstructures, Nanjing University, Nanjing 210093, China*

(Received 25 June 2021; revised 12 September 2021; accepted 16 September 2021; published 5 October 2021)

A novel planar Hall effect (PHE) is induced by the chiral anomaly or nontrivial Berry curvature, which has been predicted in nonmagnetic Weyl/Dirac semimetals. Recent theories suggest such an effect exists in three-dimensional (3D) topological insulators even in the absence of chiral anomaly. In this paper, we present a detailed analysis of the transport properties in the quasi-1D $TaSe_3$, a candidate of topological superconductor (TSC) predicted by the theorist. There are some interesting observations on $TaSe_3$. (1) The electron-hole compensation has been confirmed by the Hall effect measurements around $T_{com} \sim 30$ K, which accounts for the extremely large magnetoresistance in $TaSe_3$. (2) The remarkable PHE and anisotropic magnetoresistance (AMR) are observed in $TaSe_3$. Based on the detailed analysis of the PHE and AMR curves, the origin of PHE in $TaSe_3$ is suggested to originate from the resistivity anisotropy induced by the difference of field-induced anisotropic scattering in surface Dirac fermions of various spins. (3) We observed the successive Fermi surface reconstruction induced by the temperature around $T^* \sim 50$ K, where the amplitude of intrinsic PHE drops sharply related to the suppression of the topological surface state. Meanwhile, the $d\rho_{xx}(T)/dT$ curve presents a broad anomaly around $T_{peak} \sim 70$ K, which can be explained as a possible charge-density wave associated with imperfect Fermi surface nesting. PHE provides an effective method to understand the relationship between the electronic transport properties and the topological structure in quasi-1D TSC $TaSe_3$.

DOI: 10.1103/PhysRevB.104.155106

I. INTRODUCTION

The study of novel quantum states of matter has triggered the recent discovery of topological materials, which refreshes our understanding of condensed matter physics. Topological materials predicted by theory such as Weyl/Dirac semimetals [1,2] and topological insulators (TIs) [3,4] are effective carriers for discovering the dynamics of relativistic particles such as Dirac, Weyl, and Majorana fermions. A finite-energy gap can be observed in three-dimensional (3D) TIs, which are crossed by two gapless surface-state branches with nontrivial spin textures protected from backscattering by time-reversal symmetry. However, 2D and 1D materials only host a 1D topological edge state or local topological point states at both ends. Boundaries between distinct topological phases of 1D matter exhibit robust, yet novel quantum states. For example, Su, Schrieffer, and Heeger described chiral TIs, charge fractionalization, and spin-charge separation based on a 1D system [5,6]. The layered transition-metal trichalcogenides with formula MX_3 (M = Nb, Ta, Zr and X = S, Se, Te) are typical quasi-1D materials. Quasi-1D trichalcogenide compounds tend to form the unstable electronic structure associated with a charge-density wave (CDW), which has been confirmed in $NbSe_3$, TaS_3, and NbS_3 [7–9]. As a representative MX_3-type material, theoretical calculations excluded the existence of imaginary frequencies in phonon dispersion spectrum of $TaSe_3$ [10]. Moreover, first-principles calculations predicted that quasi-1D $TaSe_3$ exists a 3D strong TI phase with Z_2 invariants(1,100) [10]. Interestingly, transport properties measurement proved $TaSe_3$ belongs to the superconducting family with transition temperature $T_c \sim 2$ K [11], which suggests $TaSe_3$ is a potential topological superconductor (TSC) that provides us a realistic system to study the interplay between superconductivity and topological phase in the future. In addition, reversible strain-induced topological phase transitions in $TaSe_3$ have been revealed by both theoretical and experimental results [10,12], which enable $TaSe_3$ a perfect platform to engineer the topological state. However, the surface state of topological materials strongly depends on the position of the Fermi surface. Exploiting the surface transport properties of TIs is a necessary requisite. Although a recent study has identified both the inverted bulk band structure and the topological surface states (TSSs) in the bulk $TaSe_3$ band gap based angle-resolved photoemission spectroscopy (ARPES) measurements [13], the transport experiments lack any direct confirmation of surface Dirac fermions in a system. The planar Hall effect (PHE) proved to be an indication of the Weyl/Dirac nature from the perspective

*Correspondence author: xluo@issp.ac.cn
†Correspondence author: ypsun@issp.ac.cn

of transport, which has been verified in many Weyl/Dirac semimetals such as VAl_3, $MoTe_2$, TaAs, WTe_2, etc. [14–17]. In general, the planar Hall response is further related to the effect of the nontrivial Berry phase and magnetic moments. PHE might provide another key evidence on the TSS transport of quasi-1D $TaSe_3$.

PHE involves the measurement of the transverse voltage in response to the longitudinal current when the applied magnetic field and electric field all lie on the in-plane of the material. In ferromagnets, the mechanism of its origin related to PHE was eventually well established through the works of Mott [18], Smit [19], and extended by others [20]. The PHE phenomenon is well understood in diluted magnetic alloys [21], which is interpreted as the rotation of the magnetization by the in-plane magnetic field changes the distribution of unoccupied d states concerning the current direction, resulting in a change in the scattering rate of electrons in different valence bands near the Fermi surface between the s band and the d band. Previously, PHE coupled with negative magnetoresistance has been discovered and predicted in topological materials. The phenomenon that the rotating magnetic field in the plane of a sample induces oscillating transverse voltage is labeled as a fingerprint of the chiral anomaly or nontrivial Berry curvature, which may be supported by the additional transport evidence of Weyl and Dirac fermions [14,17]. However, the origin of the PHE in TIs remains unclear theoretically. Taskin *et al.* [21] employed a theory model of electron scattering off magnetic impurities polarized by an in-plane magnetic field and held that for PHE phenomenon, the magnetization of the scatterers is indispensable, as it can be explained as the anisotropic backscattering induced by magnetic disorders. However, Zheng *et al.* [22] argued that the in-plane magnetic field can tilt the Dirac cone with nonlinear momentum terms and the resulting anisotropic backscattering leads to the PHE, which is irrelevant to the magnetic nature of the scatterers. A quasiclassic theory of planar Hall conductivity due to bulk conduction in 3D strong TIs based on Boltzmann transport theory was proposed by Nandy *et al.* [23], who emphasized that such an effect also exists in 3D TIs due to the Berry curvature of the conduction band even in the absence of chiral anomaly. Recent studies on $Bi_{1.1}Sb_{0.9}Te_2S$ and $HfTe_5$ [24,25] demonstrated that PHE is attributed to the spin-momentum locking surface states of the TI with the interpretation of the difference of backscattering forbiddance induced by the in-plane magnetic field in Dirac fermions of various spins. A comprehensive and systematic explanation of the mechanism of PHE in topological materials has not yet been formed.

In this paper, we present detailed electrical transport properties on quasi-1D TSC $TaSe_3$ to study the anisotropy of its topology and electronic structure. Longitudinal magnetoresistance (LMR) under low-temperature $T = 1.8$ K and high-field $B_{max} = 33$ T showed two Shubnikov-de Haas (SdH) oscillations with two frequencies: $F_\alpha \approx 95$ T and $F_\beta \approx 166$ T associated with a nontrivial electron Fermi pocket and a nontrivial hole Fermi pocket in the Brillouin zone, respectively. Angle-dependent quantum oscillations by rotating the sample with respect to the magnetic field provided transport evidence for the existence of TSS. Hall effect measurements on the $TaSe_3$ sample revealed that the imperfect compensation effect of electrons and holes is the origin of the unsaturated XMR below $T_{com} \sim 30$ K. In addition, the remarkable giant PHE and anisotropic magnetoresistance (AMR) were studied in detail. Although PHE and anisotropic AMR curves can be perfectly fitted by the theoretical equations, we proved that the anisotropic PHE is suggested to originate from resistivity anisotropy induced by the difference of field-induced anisotropic scattering in Dirac fermions of various spins, instead of the chiral anomaly that leads to negative magnetoresistance. Meanwhile, we observed the dominant carriers change from n-type to p-type near $T^* \sim 50$ K, where the amplitude of intrinsic PHE drops sharply related to the suppression of TSS. The $d\rho_{xx}(T)/dT$ curves presenting a broad anomaly around $T_{peak} \sim 70$ K can be explained as possible CDW associated with imperfect Fermi surface nesting.

II. EXPERIMENTAL DETAILS

High-quality single-crystal samples of $TaSe_3$ were prepared via the two-step chemical vapor transport method. High-purity Ta powder and Se particles with a molar ratio of 1:4, where excess Se acted as the transport agent, were mixed and sealed in a quartz tube. First, the pellet was sealed in an evacuated quartz tube and placed into a two-zone furnace with a gradient from 710 to 650°C. The end of the quartz tube with the starting raw material was heated up to 650°C for 10 h. Meanwhile, the other end of the tube furnace heated to 710°C, thus creating an inverse temperature gradient for the synthesis of $TaSe_3$ polycrystalline powder at the source end for 50 h. In the subsequent hour, the temperature of the raw material end and the growth end was exchanged quickly so that the quartz tube was placed in a forward temperature gradient for the $TaSe_3$ crystal growth. The furnace program was maintained for 3 weeks, then turned off, and the quartz tube was allowed to cool slowly to room temperature. Finally, ribbonlike $TaSe_3$ single crystals with a typical dimension of $10 \times 0.5 \times 0.1\, mm^3$ can be obtained.

Single-crystal x-ray diffraction (XRD) measurements of $TaSe_3$ were performed on the PANalytical X' Pert diffractometer with Cu K_α radiation ($\lambda = 0.15406$ nm) at room temperature. The component characterization was determined on the commercial energy dispersive spectroscopy (EDS) equipped with a Hitachi SU8000 Series scanning electron microscope. The EDS measurements were carried out at more than 10 different points on the crystals to characterize that the selected single-crystal sample were uniform. Longitudinal resistivity and traditional/planar Hall were measured using the standard seven-probe method in a Quantum Design Physical Properties Measurement System (PPMS-9T). High-field MR oscillation was carried out at the High Magnetic Field Laboratory of the Chinese Academic Sciences (water-cooling magnet WM-5, $H = 35$ T). The planar Hall, ordinary Hall, and high-field MR oscillation data were all obtained from the same sample.

III. RESULTS AND DISCUSSIONS

The XRD pattern at room temperature by a conventional $\theta - 2\theta$ scan for $TaSe_3$ single crystal is shown in Fig. 1(a), in which we can observe peaks arising from $(1\,0\,\bar{1})$ planes, consistent with a monoclinic structure with the $P2_1/m$ space

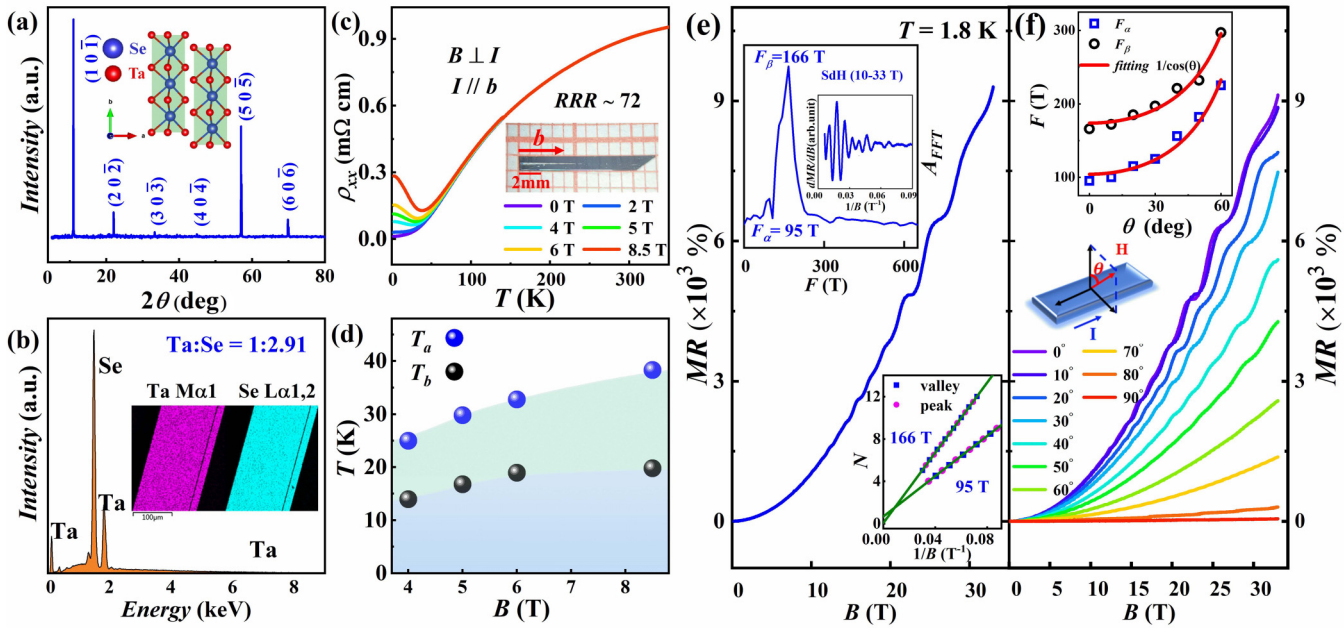

FIG. 1. (a) Single crystal XRD pattern of $TaSe_3$ single crystal. Inset: The quasi-1D crystal structure of $TaSe_3$. (b) The EDS spectrum of the $TaSe_3$ crystal. Insets: The EDS mapping pictures of Ta and Se, respectively. (c) Temperature dependence of the longitudinal resistivity ρ_{xx} at fixed magnetic fields. Inset: Typical $TaSe_3$ single crystal picture. (d) T-B phase diagram of $TaSe_3$ single crystal where T_a (blue sphere) is defined as the point where $\partial\rho_{xx}(T,H)/\partial T = 0$ and T_b (black sphere) is defined as the minimum of $\partial\rho_{xx}(T,H)/\partial T = 0$. (e) Magnetic-field-dependent MR at 1.8 K. Upper left inset: SdH patterns as a function of $1/B$ after subtracting the smooth background of MR and corresponding FFT spectrum of the oscillations at 1.8 K. Lower right inset: Landau index N plotted against $1/B$ at 1.8 K. Squares represent the valley positions and circles represent the peak positions of the SdH oscillations. (f) The magnetic field dependence of MR at various θ when $T = 1.8$ K. Inset shows the schematic measurement configuration. Inset: Quantum oscillatory frequencies as a function of the angle θ between B and the $[\bar{1}\,0\,\bar{1}]$ direction. F_α and F_β represent the experimentally fundamental frequencies, respectively. The solid lines are the results of the fittings.

group. The inset of Fig. 1(a) displays the crystal structure of $TaSe_3$ crystal composed of linear, prismatic chains along the crystallographic b axis. The Ta atom in the center of each unit cell forms covalent bonds with the surrounding six Se atoms exhibiting obvious 1D characteristics. The element analysis of the crystal samples was carried out by the EDS. As shown in Fig. 1(b), the atomic ratio of Ta:Se = 1:2.91 extracted from EDS indicates a slight amount of Se vacancy in the $TaSe_3$ sample, and corresponding EDS mapping pictures suggest the uniform distribution of the two elements in our samples. Figure 1(c) shows the temperature dependence of the longitudinal resistivity with the magnetic field B perpendicular to the $(1\,0\,\bar{1})$ plane and the electrical current I along the b axis at various temperatures range from 2 to 350 K. The longitudinal resistivity ρ_{xx} decreases with the temperature cooling down, presenting metallic conduction with the residual resistivity ratio $RRR = R(300\text{ K})/R(2\text{ K}) \approx 72$, which indicates the high quality of our single crystals. No superconductivity signal is observed above 2 K, which is consistent with previous reports [26]. The suppression of the superconducting state is due to low relatively current density, the critical current exceeds 3.0 A/mm and will suppress the superconductivity of $TaSe_3$ [27,28]. When applied B gradually increases, ρ_{xx} is enhanced, presenting insulating behavior with a plateau behavior at low temperature. This marked upturn behavior has been commonly observed in many topological materials [29,30]. Figure 1(d) shows the evolution of the transition temperature T_a and T_b as a function of the magnetic field, where T_a is identified as $\partial\rho_{xx}(T,B)/\partial T = 0$ and T_b is identified as the minimum of $\partial\rho_{xx}(T,B)/\partial T = 0$. It shows that both T_a and T_b increase with the increasing field; however, T_b quickly approaches saturation, indicating the temperature zone of the insulatorlike regime increases with the increasing magnetic field and the temperature zone of the resistivity plateau is almost unchanged [31].

Both theoretical calculation and the ARPES measurement have proved that $TaSe_3$ exists 3D strong TSS [10,13]. Hence, SdH oscillation is a very effective method to analyze its TSS and track the origin of XMR. Figure 1(e) shows the magnetic-field-dependent MR under low-temperature $T = 1.8$ K and high-field $B_{max} = 33$ T for a $TaSe_3$ single crystal when the applied magnetic field is perpendicular to the $(10\bar{1})$ plane. After subtracting the background by polynomial fitting, the intrinsic oscillation signal can be obtained. As presented in the left corner inset of Fig. 1(e), a fast Fourier transform (FFT) result displays two frequencies with $F_\alpha \approx 95$ T and $F_\beta \approx 166$ T, proving that there are at least two pockets across the Fermi level, which is similar to the previous literature frequencies [32,33]. The nontrivial Berry phase is key evidence to verify the topological structure of the material. According to the Onsager relation, the slope of the N plot should correspond to the oscillation frequency (the peak position of the SdH oscillation is defined as a half-integer Landau index, and the valley position is defined as an integer Landau index) while the intercept can be used to calculate the Berry phase [34,35]. The results are shown in the right corner inset of Fig. 1(e). The

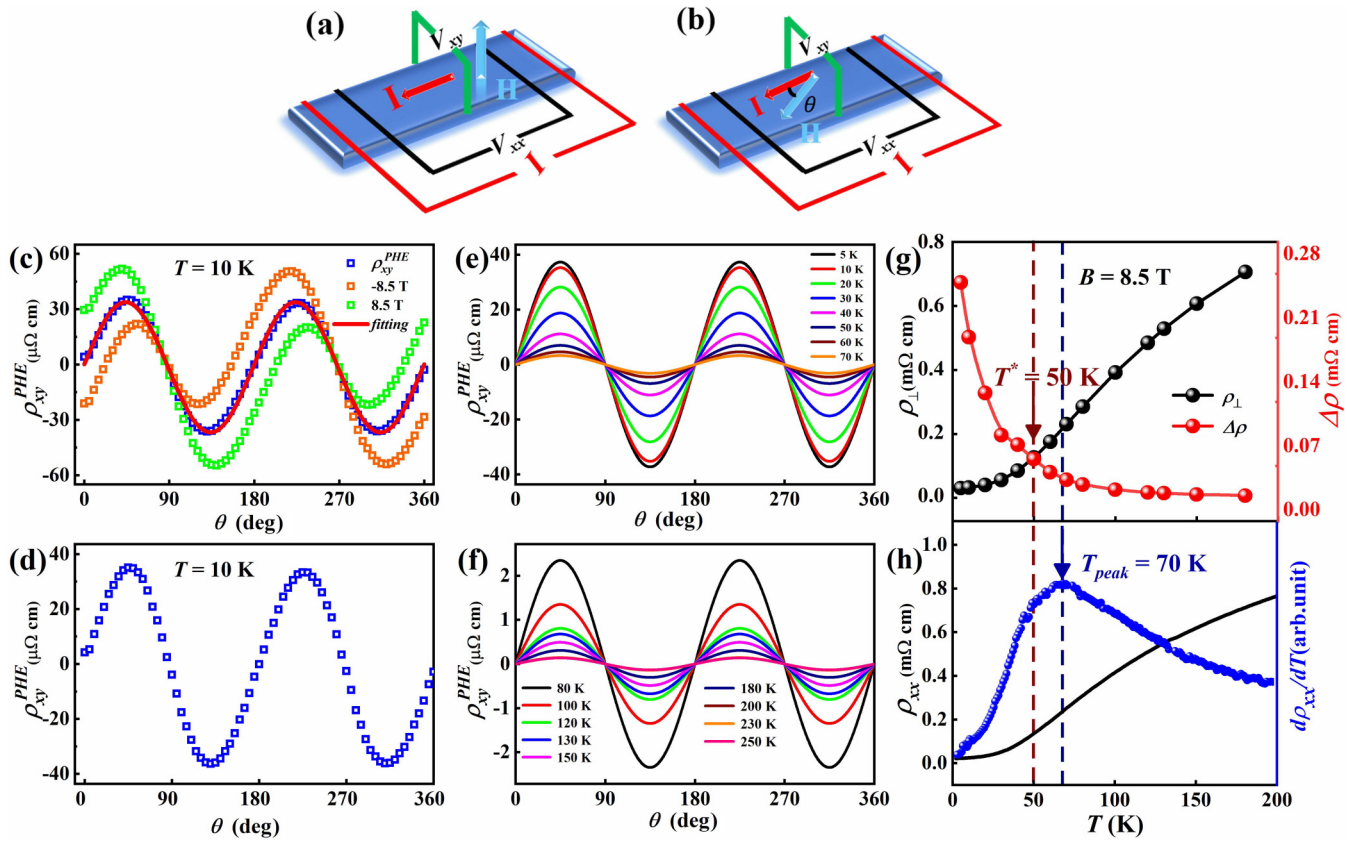

FIG. 2. (a), (b) Schematic illustrations for the ordinary and planar Hall measurement configurations. (c) The planar Hall resistivity under $B = \pm 8.5\,\mathrm{T}$ at $T = 10\,\mathrm{K}$ and the red line is the fitting result. (d) The intrinsic planar Hall resistivity at $B = 8.5\,\mathrm{T}$ after subtracting the misalignment components. (e), (f) The extracted intrinsic planar Hall resistivity versus θ at $B = \pm 8.5\,\mathrm{T}$ under various temperatures. (g) Temperature dependence of $\Delta\rho\,(\rho_\perp - \rho_\parallel)$ and $\rho_\perp$ extracted by fitting the theoretical equations. (h) ρ_{xx} and $d\rho_{xx}(T)/dT$ as a function of temperature.

slopes of the straight lines are fitted to be 94.9 and 165.5 for the α and β bands, respectively. The intercepts of 0.676 and 0.057 can be found from fitting lines, corresponding to F_α and F_β, respectively. According to band-structure calculations, the α band is an electronlike pocket with the 2D characteristic, and β band is a holelike pocket with the 3D characteristic [10]. Thus, we can obtain $\phi^\alpha(2\mathrm{D}) = 0.676 \times 2\pi \approx 1.352\pi$ and $\phi^\beta(3\mathrm{D}) = (0.057 - 1/8) \times 2\pi \approx -0.136\pi$ indicating that a nontrivial topology for the α band and a nontrivial topology for the β band. In the practical experiments, scattering from impurities and electrode contact is almost inevitable, resulting in different SdH oscillation frequencies of different samples with different qualities. The oscillation frequencies reported earlier are higher than ours, which may be affected by anisotropic scattering rates [26,33]. To further analyze the anisotropic nature of the band structure of $TaSe_3$, we measured the magnetic-field-dependent MR at various θ when $T = 1.8$ K; the results are shown in Fig. 1(f). The inset shows the schematic measurement configuration that took place from the magnetic field perpendicular to the sample surface $\theta = 0^\circ$ to the field parallel to the current direction $\theta = 90^\circ$. By FFT operation, the angle dependence of extracted oscillation frequency measured at different angles ranging from 0° to 60° is presented in the inset of Fig. 1(f). For $70^\circ \leqslant \theta \leqslant 90^\circ$, the oscillations are not resolved because of the weak SdH oscillation signal. The fitting curves of F_α and F_β are consistent with the $1/cos(\theta)$ relationship demonstrating a strict 2D behavior of the oscillations contributed by the TSS [36].

Next, we proceed to explore the PHE and AMR of $TaSe_3$. Figures 2(a) and 2(b) present schematic illustrations for the traditional and planar Hall measurement device, respectively. As is shown, for ordinary Hall effect measurement configuration, the magnetic field B always lies perpendicular to the $TaSe_3$ sample plane; in the PHE case, the magnetic field was applied parallel to the single crystal $(10\bar{1})$ plane and was rotated within the single crystal plane consecutively. The angle θ between the field and the current direction is defined in Fig. 2(b) (the initial magnetic field is perpendicular to the current direction). The chiral anomaly induced PHE ρ_{xy}^{PHE} and related AMR ρ_{xx} mathematically is formulated as [37,38]:

$$\rho_{xx} = \rho_\perp - (\rho_\perp - \rho_\parallel)\cos^2\theta \tag{1}$$

$$\rho_{xy}^{\mathrm{PHE}} = (\rho_\perp - \rho_\parallel)\cos\theta\sin\theta, \tag{2}$$

where $\rho_\parallel$ and $\rho_\perp$ is defined as resistivity corresponding to $B \parallel I$ and $B \perp I$, respectively. Note that the PHE is not just caused by the chiral anomaly as predicted by the theory. Actually, the PHE can be observed as long as the resistivity is anisotropic. The PHE can be induced by various mechanisms including chiral anomaly, classical orbital magnetoresistance

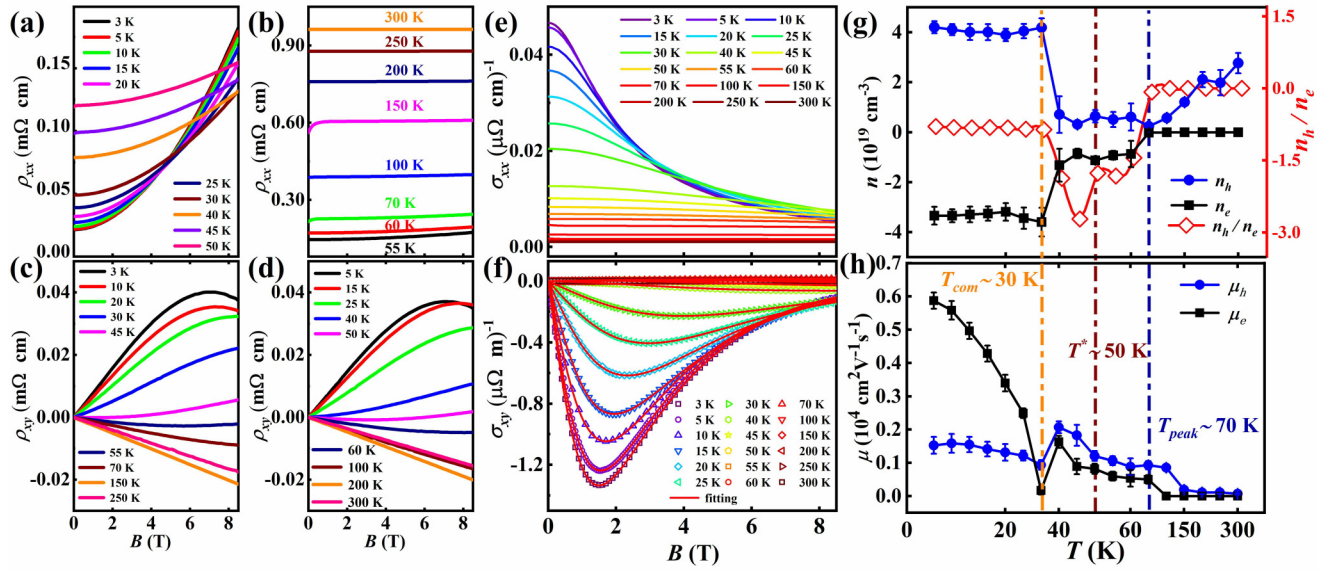

FIG. 3. (a), (b) The field dependence of longitudinal resistivity ρ_{xx} at various temperatures. (c),(d) The field dependence of Hall resistivity ρ_{xy} at various temperatures. (e) The field dependence of longitudinal conductivity σ_{xx} at various temperatures. (f) The field dependence of Hall conductivity σ_{xy} at various temperatures. The red solid lines represent the fitting results by a two-band model. (g), (h) The temperature-dependent carrier density n and the mobility μ.

(OMR), strong spin-orbital coupling and TSS, etc. [22,39]. The origin of PHE in TIs needs to be further analyzed and clarified. Due to a possible misalignment of the experimental plane of rotation with respect to the single crystal plane, the obtained PHE curves contain the contribution from the normal Hall signal and the planar Hall signal. Fortunately, the chiral anomaly induced giant PHE violates the antisymmetry rule under the opposite field. We can calculate average resistivity under the positive and negative fields to extract the PHE signal with the following equation:

$$\rho_{xy}^{\mathrm{PHE}} = [\rho_{xy}(B,\theta) + \rho_{xy}(-B,\theta)]/2. \tag{3}$$

Figure 2(c) displays the angle-dependent average Hall resistivity under $B = \pm 8.5\,\mathrm{T}$ at $T = 10$ K. Although we have subtracted the ordinary Hall component, it is clearly found that the ρ_{xy}^{PHE} does not exactly satisfy a $(\sim \sin\theta\cos\theta)$ tendency. This is due to the transverse Hall-bar misalignment will lead to a small AMR component $(-b\cos^2\theta)$ and longitudinal offset [40,41]. Therefore, we can subtract this small longitudinal resistivity by fitting the ρ_{xy}^{PHE} [15]:

$$\rho_{xy}^{\mathrm{PHE}} = a\sin\theta\cos\theta + b\cos^2\theta + c. \tag{4}$$

As shown in Fig. 2(d), after subtracting the effect originating from the experimental misalignments, the obtained intrinsic PHE ρ_{xy}^{PHE} displays $\backsim \cos\theta\sin\theta$ tendency, which is consistent with theoretical prediction. Subsequently, we conducted the measurements on the angle dependence of planar Hall resistance at various temperatures ranging from 5 to 250 K under $B = \pm 8.5\,\mathrm{T}$ to further investigate the evolution of the amplitude of intrinsic PHE in $TaSe_3$ with decreasing temperature; the angle dependence of PHE amplitudes is curved in Figs. 2(e) and 2(f) (raw PHE resistance data and fitting results can be found in the Supplemental Material [42]). Subsequently, we fit the longitudinal resistivity and the planar Hall resistivity by using Eqs. (1) and (2). As shown in Fig. 2(g), we present the temperature dependence of the chiral anomaly induced resistivity anisotropy $\Delta\rho$ $(\rho_\perp - \rho_\parallel)$ and $\rho_\perp$. As the temperature increases, PHE amplitude gradually decreases at the temperature from 5 to 70 K until it is completely suppressed near 70 K and PHE amplitude becomes saturated above 70 K; however, $\rho_\perp$ exhibits the opposite change behavior, which results in a significant intersection near $T^* \sim 50\,\mathrm{K}$. Interestingly, the $\mathrm{d}\rho_{xx}/\mathrm{d}T$ curve also shows a broad peak near $T_{\mathrm{peak}} \sim 70\,\mathrm{K}$ displayed in Fig. 2(h). A sudden upturn around this temperature region suggests a reconstruction of the Fermi surface which may be related to CDW originating from temperature-induced possible crystal structure parameters [31]. Theoretically, the formation of the CDW will cause the folding of the Fermi surface, which may influence the nontrivial band structure [10]. Specifically, for a system with the chiral anomaly, it is related to coupling and competition between the chiral charge and the electric one [15]. Therefore, it is necessary to further explore the origin of the PHE phenomenon.

To further capture the $TaSe_3$ Fermi surface modulation effect, the Hall effect measurement has been carried out on the $TaSe_3$ single crystal. Figures 3(a)–3(d) display ρ_{xx} and ρ_{xy} as a function of the magnetic field for a fixed temperature ranges from 3 to 300 K. Significant nonlinear behavior of ρ_{xy} can be observed from 3 to 50 K. The nonlinear behavior of ρ_{xy} at low temperatures without showing any sign of saturation at high fields is usually involved anomalous Hall effect (AHE), which often originates from scattering effects and the intrinsic contribution connected with the Berry curvature. Similar nonlinear Hall traces can be observed in nonmagnetic topological materials Cd_3As_2 and $ZrTe_5$ and interpreted as originating from the nonvanishing Berry curvature induced by combining large Zeeman splitting and strong spin-orbit coupling [43–45]. The origin of the AHE in the nonmagnetic

topological materials remains to be unambiguously and quantitatively clarified. The widely used two-band model tends to interpret nonlinearity as the presence of more than one type of carrier. The longitudinal conductivity $\sigma_{xx} = \rho_{xx}/(\rho_{xx}^2 + \rho_{xy}^2)$ and Hall conductivity $\sigma_{xy} = \rho_{yx}/(\rho_{xx}^2 + \rho_{xy}^2)$ can be obtained from the original experimental data further. The conductivity of σ_{xx} and σ_{xy} can be further analyzed by the semiclassical two-band model [31] referred to contributions from holelike and electronlike carriers:

$$\sigma_{xx} = \frac{en_e\mu_e}{1+(\mu_e B)^2} + \frac{en_h\mu_h}{1+(\mu_e B)^2} \tag{5}$$

$$\sigma_{xy} = -\sigma_{yx} = \left[\frac{n_e{\mu_e}^2}{1+(\mu_e B)^2} - \frac{n_h{\mu_h}^2}{1+(\mu_h B)^2}\right]eB. \tag{6}$$

As presented in Figs. 3(g) and 3(h), the carrier concentrations and mobilities are obtained from fitting results based on the two-band model. There are some interesting observations on $TaSe_3$ from Hall measurement results. Under relatively low temperature below 30 K, the ratio of carrier concentrations $n_h/n_e \approx 0.8$ suggests that imperfect electron-hole compensation may account for XMR in $TaSe_3$. As the temperature increases, the slope of ρ_{xy} changes from positive to negative near 50 K indicates that the dominant carriers change from p-type to n-type around $T^* \sim 50$ K. The temperature-dependent curves of carrier concentrations n and mobilities μ become discontinuous between 30 and 50 K. From our observations, there may exist a possible electric phase transition around $T^* \sim 50$ K, and the Fermi surface reconstruction induced by the temperature plays an important role in the transport properties of $TaSe_3$. In addition, the $d\rho_{xx}(T)/dT$ curve presents a broad anomaly around $T_{\text{peak}} \sim 70$ K and can be explained as possible CDW associated with imperfect Fermi surface nesting. Interestingly, recent studies on the dimensional control of $TaSe_3$ nanowires, uniaxial stress, and Cu-doping control about the transport properties of $TaSe_3$ have observed anomalous resistance near 70 K, indicating that although $TaSe_3$ exists quasi-1D trigonal prismatic chains the same as other MX_3 materials, stronger coupling between the chain makes $TaSe_3$ form a more 3D crystal structure where the quasi-1D character is strongly suppressed. The dimensionality reduction of $TaSe_3$ further promotes the Peierls instabilities leading to the CDW transition [27,46,47]. Due to the imperfect one-dimensionality of the $TaSe_3$ lattice structure, imperfect Fermi surface nesting leading to the insufficient opening of the CDW gap may be the reason why the electric transport behavior of CDW is not obvious. This requires more structural characterization and theoretical calculations to verify. It can be seen that the significant transition point of PHE amplitude based on the theory of chiral anomaly is relevant to the CDW transition point obtained by electrical transport measurement in $TaSe_3$. In addition, the planar Hall resistivity of the No. 2, No. 3, and No. 4 $TaSe_3$ crystals with different amounts of Se vacancies can be found in the Supplemental Material [42] (see also Refs. [17,38,48–50] therein). The results show that all the PHE curves exhibit the $cos\theta sin\theta$ dependence, but the transition temperature T^* of $TaSe_3$ samples with different amounts of Se vacancies varies from 41 to 50 K. This may be due to the chemical potential of samples with different defects. The difference in single-crystal quality slightly affects the topological band structure near the $TaSe_3$ Fermi surface, which needs to be further studied.

To clarify the relationship between these two physical mechanisms and explore the origin of the PHE, we further tracked the field dependence of the extracted amplitude of PHE under different magnetic fields at $T = 5$, 20, and, 50 K. The relationship between the PHE curve and the angle is given in Figs. 4(a), 4(c), and 4(e), respectively. For the weak magnetic field limit, ρ_{xy}^{PHE} follows the below equation [48,51]:

$$\rho_{xy}^{\text{PHE}} \propto (L_c/L_a)^2 \sin\theta\cos\theta, \tag{7}$$

where $L_a = D/\Gamma B$ are the parameters related to the magnetic field with diffusion coefficient D and Γ. The transport coefficient $L_c = \sqrt{D\tau_c}$ is the chiral diffusion length with the scattering time of chiral charge τ_c. The amplitudes of PHE versus B are shown in Figs. 4(b), 4(d), and 4(f), and the fitting amplitudes of PHE exhibit quadratic law $\sim B^2$ at $T =$ 5, 20, and 50 K, which satisfies the weak magnetic field limit, $L_a \ll L_c$.

Until now, it seems we can conclude that the curves of PHE can be well interpreted by the theoretical equations based on the chiral anomaly. However, there is still confusion that has not been clarified: (1) The PHE effect induced by chiral anomaly is generally accompanied by negative longitudinal MR in topological semimetal. In addition, previous theoretical work showed that the PHE effect exists also in 3D TIs due to the Berry curvature of the conduction band even without chiral anomaly [21]. (2) The OMR can significantly enhance the anisotropic resistivity $\rho_\parallel - \rho_\perp$ that always produces a PHE curve the same with the chiral anomaly induced PHE. (3) As Pippard's framework of normal MR also has demonstrated that the MR shows varying dependence for different scales such as $\omega_c\tau$, μB [51], it remains to be explored whether the behavior of the B-T curves exhibiting the power exponent approaches 2 is related to the chiral anomaly or simply originating from high mobility. Therefore, we need to further verify the $\Delta\rho$ under different temperatures and magnetic fields. The AMR curves, with the rotating in-plane magnetic field presenting the angle dependence with a period of 180 at $T = 5$ and 50 K, are shown in Figs. 5(a) and 5(b). Notably, all the ρ_{xx} curves follow strictly the $\cos^2\theta$ tendency, which indicates that the AMR signal mainly comes from the rotating in-plane field instead of the traditional LMR caused by the out-of-plane magnetic field component, because the slight misalignment of the sample is unavoidable. Figures 5(c) and 5(d) show the parametric plots of the $TaSe_3$ by plotting ρ_{xx} and ρ_{xy} with angle φ as the parameter under the various field. In a system dominated by the chiral anomaly such as GdPtBi and Na_3Bi [52], a concentric orbits pattern with the increasing field in the parametric plots can be observed. By contrast, in our measurement of $TaSe_3$, the orbits evolve to a "shock wave" with B increases that indicate that higher mobility creates exaggerated skewing of the rightward expansion. This phenomenon excludes the chiral anomaly induced PHE in our sample. Figures 5(e) and 5(f) exhibit extracted parameters connected to $\rho_\parallel$ and $\rho_\perp$ at $T = 5$ and 50 K from the fitting results by using Eq. (1); $\Delta\rho = (\rho_\perp - \rho_\parallel)$ can be further fitted to power-law curves $\Delta\rho \sim B^{1.87}$ and $\Delta\rho \sim B^{1.96}$, respectively. There are some differences in the behavior of $\rho_\parallel$ and $\rho_\perp$ at

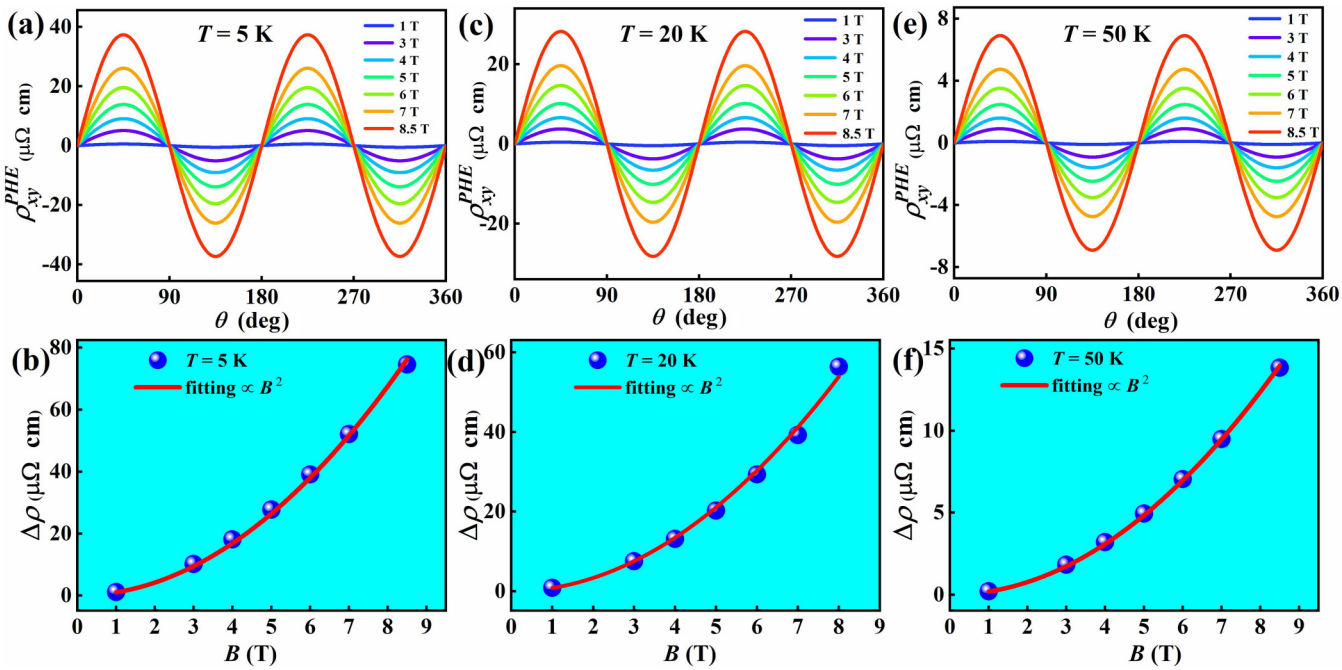

FIG. 4. (a), (c), (e) The extracted intrinsic planar Hall resistivity versus θ at $T = 5$, 20 and 50 K under different fields. (b), (d), (f) Magnetic-field dependence of the amplitudes of PHE at $T = 5$, 20, and 50 K under different fields. The red lines represent the fitting results following quadratic dependence.

two different temperatures with the increasing B as presented in the insets; $\rho_\perp$ rises rapidly, but $\rho_\parallel$ increases in a moderate way especially at 50 K, which means the main contribution of the increased $\Delta\rho$ mainly comes from the rapid increase of $\rho_\perp$ instead of the decrease of $\rho_\parallel$, which contradicts the mechanism of PHE induced by the chiral anomaly. Moreover, we can extract important information from Figs. 5(e) and 5(f). The intersection of the extension lines of $\rho_\perp$ and $\rho_\parallel$ is the value of ρ_{xx} at zero magnetic field, which is consistent with the $\rho_{xx} - T$ curve. Second, the $\rho_\perp$ is positively correlated

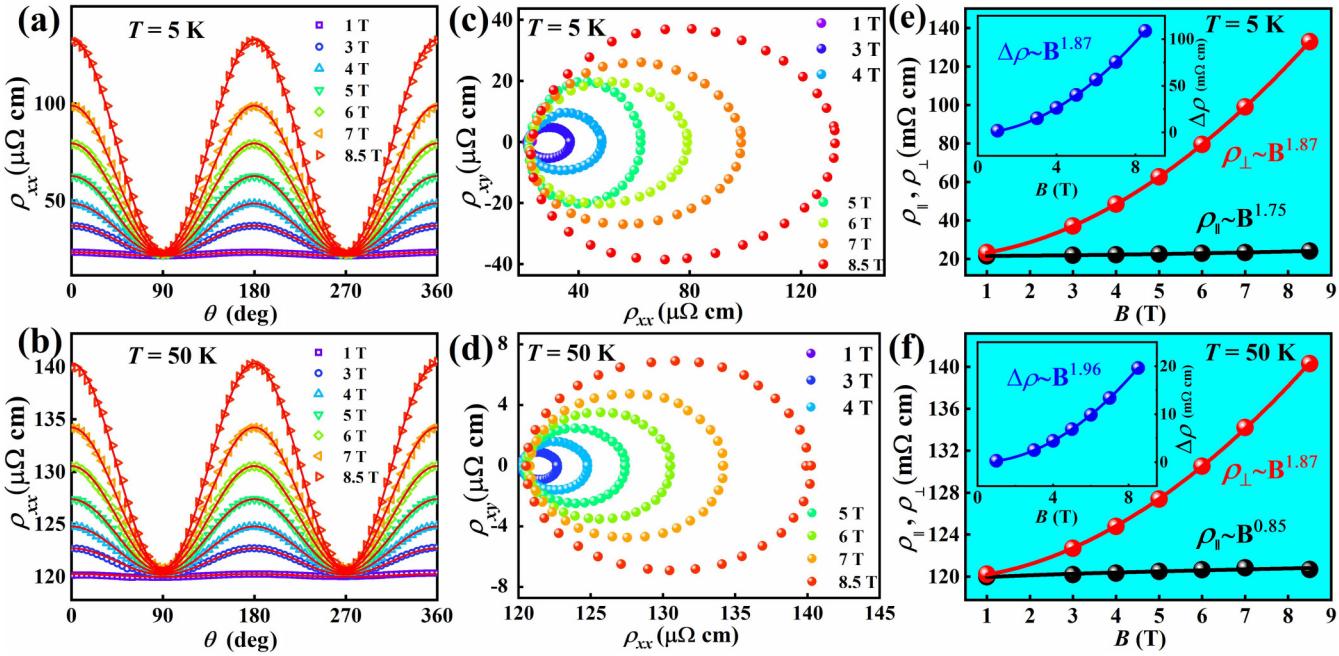

FIG. 5. (a), (b) In-plane AMR versus angle θ at fixed fields ($T = 5$ and 50 K). Solid red curves represent the fitting curves by using Eq. (1). (c), (d) Parametric plots of PHE in the $TaSe_3$ single crystal. The orbits obtained by plotting ρ_{xx} and ρ_{xy} with angle θ as the parameter at specific magnetic fields. (e), (f) Magnetic field dependence of $\rho_\parallel$ and $\rho_\perp$ obtained by fitting Eqs. (1) and (2). Solid curves are power law fitting results. Inset: Magnetic field dependence of $\Delta\rho$.

with the magnetic field in the entire magnetic field, which suggests the chiral anomaly is suppressed by another factor that induces a positive longitudinal magnetoresistance [41]. Therefore, the evolutionary behavior $\rho_{\perp}$ increases quickly, but $\rho_{\parallel}$ increases slowly, which indicates that the large anisotropic OMR is the origin of PHE. The signature of chiral anomaly is fully covered by the OMR.

Next, we discuss the possible physical mechanisms related to anisotropic resistivity that lead to the PHE phenomenon in $TaSe_3$. Our experiment results showed that there is no negative magnetoresistance in $TaSe_3$. In addition, the $\rho_{xx} - \rho_{xy}$ parametric plot exhibits a "shock-wave" pattern, indicating the significant difference in mobility creates conditions for anisotropic PHE resistivity. The mechanism of chiral anomaly is ruled out. At the same time, we observed the successive Fermi surface reconstruction induced by the temperature around $T^* \sim 50\,\mathrm{K}$, where the amplitude of intrinsic PHE drops sharply. Therefore, we attribute significant changes in PHE amplitudes to the change in the topological electronic band structures. The temperature-dependent anisotropy could be induced by the hybrid coupling of surface states where the carriers are spin-momentum locked [24,25]. For spins that are parallel or antiparallel to the magnetic field, the forbidden backscattering has little effect on resistivity $\rho_{\perp}$. In contrast, for spins that are perpendicular to the B, the allowed backscattering results in the increased resistivity $\rho_{\parallel}$. The in-plane magnetic field destroys the TSS and spin-polarizes randomly distributed impurity, which greatly changes the TI surface where the spin-momentum locking mechanism prevents Dirac fermions from backscattering in no field. A strict 2D behavior contributed by the TSS was further verified by angle-dependent SdH oscillations; results are shown in the inset of Fig. 1(f). We believe that the PHE in $TaSe_3$ stems from dominated TI surface states, and the drop at 50 K in PHE amplitude can be explained as the suppression of TSS. Although the quasi-1D $TaSe_3$ has a naturally low bulk/surface ratio, disentangling the bulk and the surface states has always been a challenge experimentally. The emergence of PHE in bulk-dominated TI establishes that the PHE does not necessarily require surface-state transport. For example, Nandy *et al.* [21] showed that the PHE phenomenon in the bulk limit TSs can be induced by Berry curvature of the conduction band even in the absence of chiral anomaly, which indicates that the contribution of bulk states to PHE in TIs could be significant. This calls for theoretical calculations that attribute PHE to the band structure of $TaSe_3$ and experiments about the PHE phenomenon of $TaSe_3$ films with different thicknesses to further verify. In addition, Zheng *et al.* [22] proposed a nontopological origin and emphasized that anisotropic backscattering can arise from the tilt of the Dirac cone by an in-plane magnetic field, which is irrelevant to the magnetic nature of the scatterers. This theory needs to be verified by PHE experiments in different directions. We believe that the PHE amplitude strongly depends on the position of the Fermi surface, the control of the chemical potential position via quantum engineering, such as chemical doping, tuning the carrier concentration, or external pressure to explore the origins of the PHE phenomenon about $TaSe_3$, which is necessary requisite.

In summary, we present a detailed analysis of the transport properties of 1D $TaSe_3$. The electron-hole compensation has been found around $T_{\mathrm{com}} \sim 30\,\mathrm{K}$ where XMR occurs in $TaSe_3$, which is confirmed by Hall measurement. Meanwhile, we observe remarkable PHE and AMR in $TaSe_3$ with TSS further verified by angle-dependent SdH oscillations results. The PHE amplitude in $TaSe_3$ is robust and still visible at $T = 250\,\mathrm{K}$. The successive Fermi surface reconstruction is induced by the temperature around $T^* \sim 50\,\mathrm{K}$, where the amplitude of intrinsic PHE drops sharply related to the suppression of TSS. We observed the anomalies of $d\rho_{xx}(T)/dT$ curves around $T_{\mathrm{peak}} \sim 70\,\mathrm{K}$, which can be explained as a possible CDW associated with imperfect Fermi surface nesting. In addition, based on the detailed analysis of the PHE and AMR curves, the origin of PHE in $TaSe_3$ is well discussed: The $\rho_{xx} - \rho_{xy}$ parametric plot exhibits a "shock-wave" pattern. In addition, based on the analysis of the in-plane AMR, negative longitudinal MR is not observed. All the evidence indicated that the presented PHE in $TaSe_3$ originates from the trivial orbital magnetoresistance caused by the magnetic scattering mechanism of the TSS rather than the topological-nontrivial chiral anomaly. We prove that PHE will provide another golden criterion to study the TSSs and that our experiments will pave the way for further theoretical modeling regarding the investigation of anisotropies leading to PHE in TIs.

ACKNOWLEDGMENTS

This work was supported by the Joint Funds of the National Natural Science Foundation of China and the Chinese Academy of Sciences' Large-Scale Scientific Facility under Contracts No. U1932217 and No. U1832141, the National Key Research and Development Program under Contract No. 2016YFA0300404, and the National Nature Science Foundation of China under Contracts No. 11674326 and No. 11874357.

[1] Z. K. Liu, B. Zhou, Y. Zhang, Z. J. Wang, H. M. Weng, D. Prabhakaran, S. K. Mo, Z. X. Shen, Z. Fang, X. Dai, Z. Hussain, and Y. L. Chen, Science **343**, 864 (2014).

[2] B. Q. Lv, N. Xu, H. M. Weng, J. Z. Ma, P. Richard, X. C. Huang, L. X. Zhao, G. F. Chen, C. E. Matt, F. Bisti, V. N. Strocov, J. Mesot, Z. Fang, X. Dai, T. Qian, M. Shi, and H. Ding, Nat. Phys. **11**, 724 (2015).

[3] Y. L. Chen, J. G. Analytis, J. H. Chu, Z. K. Liu, S. K. Mo, X. L. Qi, H. J. Zhang, D. H. Lu, X. Dai, Z. Fang, S. C. Zhang, I. R. Fisher, Z. Hussain, and Z. X. Shen, Science **325**, 178 (2009).

[4] H. Zhang, C.-X. Liu, X.-L. Qi, X. Dai, Z. Fang, and S.-C. Zhang, Nat. Phys. **5**, 438 (2009).

[5] O. Gröning, S. Wang, X. Yao, C. A. Pignedoli, G. Borin Barin, C. Daniels, A. Cupo, V. Meunier, X. Feng, A. Narita, K. Müllen, P. Ruffieux and R. Fasel, Nature (London) **560**, 209 (2018).

[6] E. J. Meier, F. A. An, and B. Gadway, Nat. Commun. **7**, 13986 (2016).

[7] R. V. Coleman, G. Eiserman, M. P. Everson, A. Johnson, and L. M. Falicov, Phys. Rev. Lett. **55**, 863 (1985).

[8] G. Grüner, Rev. Mod. Phys. **60**, 1129 (1988).

[9] Z. Z. Wang, P. Monceau, H. Salva, C. Roucau, L. Guemas, and A. Meerschaut, Phys. Rev. B **40**, 11589 (1989).

[10] S. Nie, L. Xing, R. Jin, W. Xie, Z. Wang, and F. B. Prinz, Phys. Rev. B **98**, 125143 (2018).

[11] T. Sambongi, M. Yamamoto, K. Tsutsumi, Y. Shiozaki, K. Yamaya, and Y. Abe, J. Phys. Soc. Jpn. **42**, 1421 (1977).

[12] C. Lin, M. Ochi, R. Noguchi, K. Kuroda, M. Sakoda, A. Nomura, M. Tsubota, P. Zhang, C. Bareille, K. Kurokawa, Y. Arai, K. Kawaguchi, H. Tanaka, K. Yaji, A. Harasawa, M. Hashimoto, D. Lu, S. Shin, R. Arita, S. Tanda, and T. Kondo, Nat. Mater. **20**, 1093 (2021).

[13] C. Chen, A. Liang, S. Liu, S. Nie, J. Huang, M. Wang, Y. Li, D. Pei, H. Yang, H. Zheng, Y. Zhang, D. Lu, M. Hashimoto, A. Barinov, C. Jozwiak, A. Bostwick, E. Rotenberg, X. Kou, L. Yang, Y. Guo *et al.*, Matter **3**, 2055 (2020).

[14] R. Singha, S. Roy, A. Pariari, B. Satpati, and P. Mandal, Phys. Rev. B **98**, 081103(R) (2018).

[15] F. C. Chen, X. Luo, J. Yan, Y. Sun, H. Y. Lv, W. J. Lu, C. Y. Xi, P. Tong, Z. G. Sheng, X. B. Zhu, W. H. Song, and Y. P. Sun, Phys. Rev. B **98**, 041114(R) (2018).

[16] Q. R. Zhang, B. Zeng, Y. C. Chiu, R. Schonemann, S. Memaran, W. Zheng, D. Rhodes, K.-W. Chen, T. Besara, R. Sankar, F. Chou, G. T. McCandless, J. Y. Chan, N. Alidoust, S.-Y. Xu, I. Belopolski, M. Z. Hasan, F. F. Balakirev, and L. Balicas, Phys. Rev. B **100**, 115138 (2019).

[17] P. Li, C. Zhang, Y. Wen, L. Cheng, G. Nichols, D. G. Cory, G.-X. Miao, and X.-X. Zhang, Phys. Rev. B **100**, 205128 (2019).

[18] N. F. Mott, Proc. Roy. Soc. **A153**, 699 (1936).

[19] J. Smit, Physica **17**, 612 (1951).

[20] I. A. Campbell, A. Fert, and O. Jaoul, J. Phys. C **3**, S95 (1970).

[21] A. A. Taskin, H. F. Legg, F. Yang, S. Sasaki, Y. Kanai, K. Matsumoto, A. Rosch, and Y. Ando, Nat. Commun. **8**, 1340 (2017).

[22] S.-H. Zheng, H.-J. Duan, J.-K. Wang, J.-Y. Li, M.-X. Deng, and R.-Q. Wang, Phys. Rev. B **101**, 041408(R) (2020).

[23] S. Nandy, A. Taraphder, and S. Tewari, Sci. Rep. **8**, 14983 (2018).

[24] B. Wu, X.-C. Pan, W. Wu, F. Fei, B. Chen, Q. Liu, H. Bu, L. Cao, F. Song, and B. Wang, Appl. Phys. Lett. **113**, 011902 (2018).

[25] P. Wang, T. Hou, F. Tang, P. Wang, Y. Han, Y. Ren, H. Zeng, L. Zhang, and Z. Qiao, Chin. Phys. Lett. **38**, 017201 (2021).

[26] Y. Zhang, T. Zhu, H. Bu, Z. Cai, C. Xi, B. Chen, B. Wei, D. Lin, H. Xie, M. Naveed, X. Xi, F. Fei, H. Zhang, and F. Song, AIP Adv. **10**, 095314 (2020).

[27] J. Yang, Y. Q. Wang, R. R. Zhang, L. Ma, W. Liu, Z. Qu, L. Zhang, S. L. Zhang, W. Tong, L. Pi, W. K. Zhu, and C. J. Zhang, Appl. Phys. Lett. **115**, 033102 (2019)

[28] S. Nagata, H. Kutsuzawa, S. Ebisu, H. Yamamura, and S. Taniguchi, J. Phys. Chem. Solids **50**, 703 (1989).

[29] Y.-Y. Wang, Q.-H. Yu, P.-J. Guo, K. Liu, and T.-L. Xia, Phys. Rev. B **94**, 041103(R) (2016).

[30] Y. L. Wang, L. R. Thoutam, Z. L. Xiao, J. Hu, S. Das, Z. Q. Mao, J. Wei, R. Divan, A. Luican-Mayer, G. W. Crabtree, and W. K. Kwok, Phys. Rev. B **92**, 180402(R) (2015).

[31] X. Luo, R. C. Xiao, F. C. Chen, J. Yan, Q. L. Pei, Y. Sun, W. J. Lu, P. Tong, Z. G. Sheng, X. B. Zhu, W. H. Song, and Y. P. Sun, Phys. Rev. B **97**, 205132 (2018).

[32] W. Xia, X. Shi, Y. Zhang, H. Su, Q. Wang, L. Ding, L. Chen, X. Wang, Z. Zou, N. Yu, L. Pi, Y. Hao, B. Li, Z. Zhu, W. Zhao, X. Kou, and Y. Guo, Phys. Rev. B **101**, 155117 (2020).

[33] A. I. U. Saleheen, R. Chapai, L. Xing, R. Nepal, D. Gong, X. Gui, W. Xie, D. P. Young, E. W. Plummer, and R. Jin, npj Quantum Mater. **5**, 53 (2020)

[34] J. Hu, Z. J. Tang, J. Y. Liu, X. Liu, Y. L. Zhu, D. Graf, K. Myhro, S. Tran, C. N. Lau, J. Wei, and Z. Q. Mao, Phys. Rev. Lett. **117**, 016602 (2016).

[35] T. Liang, Q. Gibson, M. N. Ali, M. Liu, R. Cava, and N. Ong, Nat. Mater. **14**, 280 (2015).

[36] D.-X. Qu, Y. S. Hor, J. Xiong, R. J. Cava, and N. P. Ong, Science **329**, 821 (2010).

[37] J. Yan, X. Luo, J. J. Gao, H. Y. Lv, C. Y. Xi, Y. Sun, W. J. Lu, P. Tong, Z. G. Sheng, X. B. Zhu, W. H. Song, and Y. P. Sun, J. Phys.: Condens. Matter **32**, 315702 (2020).

[38] A. A. Burkov, Phys. Rev. B **96**, 041110(R) (2017).

[39] D. D. Liang, Y. J. Wang, W. L. Zhen, J. Yang, S. R. Weng, X. Yan, Y. Y. Han, W. Tong, W. K. Zhu, L. Pi, and C. J. Zhang, AIP Adv. **9**, 055015 (2019).

[40] M. Wu, G. Zheng, W. Chu, Y. Liu, W. Gao, H. Zhang, J. Lu, Y. Han, J. Zhou, W. Ning, and M. Tian, Phys. Rev. B **98**, 161110(R) (2018).

[41] H. Li, H.-W. Wang, H. He, J. Wang, and S.-Q. Shen, Phys. Rev. B **97**, 201110(R) (2018)

[42] See Supplemental Material at http://link.aps.org/supplemental/10.1103/PhysRevB.104.155106 for the raw PHE and AMR curves of samples No. 1, No. 2, No. 3, and No. 4, and the geometry of the samples and electrodes.

[43] Y. Liu, H. Wang, H. Fu, J. Ge, Y. Li, C. Xi, J. Zhang, J. Yan, D. Mandrus, B. Yan, and J. Wang, Phys. Rev. B **103**, L201110 (2021).

[44] T. Liang, J. Lin, Q. Gibson, T. Gao, M. Hirschberger, M. Liu, R. J. Cava, and N. P. Ong, Phys. Rev. Lett. **118**, 136601 (2017).

[45] T. Liang, J. Lin, Q. Gibson, S. Kushwaha, M. Liu, W. Wang, H. Xiong, J. A. Sobota, M. Hashimoto, P. S. Kirchmann, Z.-X. Shen, R. J. Cava, and N. P. Ong, Nat. Phys. **14**, 451 (2018)

[46] A. Nomura, K. Yamaya, S. Takayanagi, K. Ichimura, and S. Tanda, Europhys. Lett. **124**, 67001 (2019).

[47] T. M. Tritt, E. P. Stillwell, and M. J. Skove, Phys. Rev. B: Condens. Matter **34**, 6799 (1986).

[48] P. Li, C. H. Zhang, J. W. Zhang, Y. Wen, and X. X. Zhang, Phys. Rev. B **98**, 121108(R) (2018).

[49] D. Huang, H. Nakamura, and H. Takagi, Phys. Rev. Research **3**, 013268 (2021).

[50] Z. Ren, A. A. Taskin, S. Sasaki, K. Segawa, and Y. Ando, Phys. Rev. B **82**, 241306(R) (2010).

[51] A. B. Pippard, *Magnetoresistance in Metals* (Cambridge University Press, Cambridge, 1989).

[52] S. Liang, J. Lin, S. Kushwaha, J. Xing, N. Ni, R. J. Cava, and N. P. Ong, Phys. Rev. X **8**, 031002 (2018).